Structural Diversity in White-Light-Emitting Hybrid Lead Bromide Perovskites
— **Source link** 〈↗〉

Lingling Mao, Peijun Guo, Mikael Kepenekian, Ido Hadar ...+5 more authors

Institutions: Northwestern University, Argonne National Laboratory, University of Rennes

Related papers:

- Intrinsic white-light emission from layered hybrid perovskites.

- One-dimensional organic lead halide perovskites with efficient bluish white-light emission.

- Self-assembly of broadband white-light emitters.

- White-Light Emission and Structural Distortion in New Corrugated Two-Dimensional Lead Bromide Perovskites

- White-Light Emission from Layered Halide Perovskites.

Structural Diversity in White-light Emitting Hybrid Lead Bromide Perovskites

Lingling Mao, Peijun Guo, Mikael Kepenekian, Ido Hadar, Claudine Katan,
Jacky Even, Richard Schaller, Constantinos Stoumpos, Mercouri Kanatzidis

Structural Diversity in White-light Emitting Hybrid Lead Bromide Perovskites

Lingling Mao[1], Peijun Guo[2], Mikaël Kepenekian[3], Ido Hadar[1], Claudine Katan[3], Jacky Even[4], Richard D. Schaller[1,2], Constantinos C. Stoumpos[1*] and Mercouri G. Kanatzidis[1*]

[1]Department of Chemistry, Northwestern University, 2145 Sheridan Road, Evanston, Illinois 60208, United States

[2]Center for Nanoscale Materials, Argonne National Laboratory, 9700 South Cass Avenue, Lemont, Illinois 60439, United States

[3]Univ Rennes, ENSCR, INSA Rennes, CNRS, ISCR (Institut des Sciences Chimiques de Rennes) − UMR 6226, Rennes F-35000, France

[4]Univ Rennes, INSA Rennes, CNRS, Institut FOTON − UMR 6082, Rennes F-35000, France

ABSTRACT: Hybrid organic-inorganic halide perovskites are under intense investigations because of their astounding physical properties and promises for optoelectronics. Lead bromide and chloride perovskites exhibit intrinsic white-light emission believed to arise from self-trap excitons (STEs). Here, we report a series of new structurally diverse hybrid lead bromide perovskites that have broadband emission at room temperature. They feature Pb/Br structures which vary from 1D face-sharing structures to 3D corner- and edge-sharing structures. Through single -crystal X-ray diffraction and low frequency Raman spectroscopy, we have identified the local distortion level of the octahedral environments of Pb^{2+} within the structures. The band gaps of these compound range from 2.92 to 3.50 eV, following the trend of "corner-sharing< edge-sharing< face-sharing". Density functional theory (DFT) calculations suggest the electronic structure is highly dependent on the connectivity mode of the $PbBr_6$ octahedra, where the edge- and corner-sharing 1D structure of $(2,6\text{-dmpz})_3Pb_2Br_{10}$ exhibits more disperse bands and smaller band gap (2.49 eV) than the face-sharing 1D structure of $(hep)PbBr_3$ (3.10 eV). Using photoemission spectroscopy, we measured the energies of the valence band of these compounds and found them to remain almost constant, while the energy of conduction bands varies. Temperature dependent PL measurements reveal the 2D and 3D compounds have narrower PL emission at low temperature (∼5K), whereas the 1D compounds have both free exciton emission and STEs emission. The 1D compound $(2,6\text{-dmpz})_3Pb_2Br_{10}$ has the highest photoluminescence quantum yield (PLQY) of 12%, owing to its unique structure that allows efficient charge carrier relaxation and light emission.
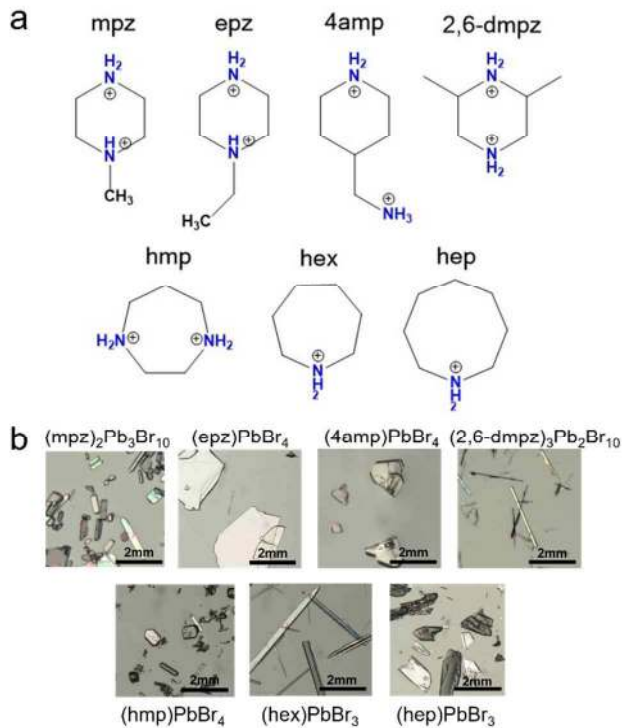
Introduction

Figure 1. (a) Organic cations used in this work. mpz =1-methylpiperazine, epz =1-ethylpiperazine, 4amp = 4-(aminomethyl)piperidine, 2,6-dmpz = 2,6-dimethylpiperazine , hmp = homopiperazine , hex = hexamethyleneimine, hep = heptamethyleneimine . (b) Optical microscopic images of the hybrid perovskite compounds synthesized using the cations listed above.

Hybrid organic-inorganic perovskites are emerging semiconducting crystalline materials that are solution-processable, low-cost and can be easily synthesized.[1-3] The diverse nature of the organic cationic templates lend these materials to be highly tunable, which, in conjunction with the variable dimensionalities of these materials ranging from single crystals to nanocrystals and thin-films,[4] have provided a solid foundation of a wide range of optoelectronic devices such as photovoltaics[5-7,8-11] and light-emitting diodes (LEDs).[12-15] Hybrid perovskites can be tuned "by design" for specific applications. The energy band gap is associated with choices of different metal ions (Pb^{2+}, Sn^{2+}, Ge^{2+}), halide anions (Cl⁻, Br⁻ and I⁻) and

the dimensionality (0D to 3D) of the structure. For the three-dimensional (3D) structures, the general formula is ABX_3, where A is methylammonium (MA^+), formamidinium (FA^+) or Cs^+, B is Pb^{2+}, Sn^{2+} or Ge^{2+}, and X is halide (Cl⁻, Br⁻ or I⁻).[16] Lowering the dimensionality to two-dimensions (2D) with corner-sharing octahedral layers and bulky organic cations separating the perovskite layers, gives rise to increased structural diversity. The general perovskite formula then becomes $A'_2A_{n-1}B_nX_{3n+1}$ (A' = 1+ cation, A = MA^+, FA^+ or Cs^+), in the Ruddlesden−Popper (RP) phases, $A'A_{n-1}M_nX_{3n+1}$,[17] in the Di-on-Jacobson phases (A' = 2+ cation, A = MA^+, FA^+ or Cs^+).[18] Further reducing the dimensionality to one-dimension (1D), the formula is then dictated by the connectivity modes of the $[BX_6]^{4-}$ octahedra, with the most common connectivity modes being face-sharing, followed by corner-sharing as well as rare edge-sharing connectivity. Notably, a single compound can have one connectivity mode or a combination of connectivity modes,[19] thus producing extremely rich and diverse structural types. Zero-dimensional (0D) compounds composed of isolated $[MX_6]^{4-}$ octahedra have also been reported, with representative examples being Cs_2SnI_6 (Sn^{4+}),[20] Cs_4PbBr_6[21-22] and possibly the mixed-metal double perovskites.[23]

Broadband white-light emission at room temperature from hybrid perovskite materials is an attractive optical property and has received tremendous attention, given the poorly understood and apparently unique photo-physics that gives rise to this phenomenon.[24] It was discovered in various (110)-oriented 2D lead bromide perovskites, such as $(C_6H_{13}N_3)PbBr_4$,[25] (N-MEDA)[$PbBr_4$][26] (N-MEDA = N1- methylethane-1,2-diammonium)[26] and (EDBE)[$PbBr_4$] (EDBE = 2,2'-(ethylenedioxy)bis(ethylammonium)).[27] Subsequent studies have focused on the correlation between the lattice distortion in order to explain the origins of the broad emission.[28-30] The currently debated broadband emission model has been connected to the highly deformed/deformable crystal lattice that induces electron-phonon coupling associated with excited states (i.e., polarons), generating the so-called self-trapped exciton (STE) states.[28] Interestingly, the broad-band emission does not only exist in layered structures, but also in lower dimensional structures, such as the recent report on 1D perovskite that exhibits bluish white-light emission and a higher photoluminescence quantum yield (PLQY) compared to the 2D perovskites.[31] Because of this, the concept of dimensional reduction[32-34] provides a new materials' design principle to

Table 1. Summary of structural characteristics and band gaps of $(2,6-dmpz)_3Pb_2Br_{10}$, $(epz)PbBr_4$, $(4amp)PbBr_4$, $(hmp)PbBr4$, $(mpz)_2Pb_3Br_{10}$, $(hep)PbBr_3$ and $(hex)PbBr_3$.

Cations	Formula	Dimensionality	space group	connectivity modes	E_g (eV)
2,6-dmpz	$(C_6H_{16}N_2)_3Pb_2Br_{10}$	1D	P-1	corner- and edge-sharing	3.16
epz	$(C_6H_{16}N_2)PbBr_4$	(110)-oriented 2D	Pc	corner-sharing	3.12
4amp	$(C_6H_{16}N_2)PbBr_4$	(100)-oriented 2D	$Pca2_1$	corner-sharing	2.92
mpz	$(C_5H_{14}N_2)_2Pb_3Br_{10}$	three-layered 2D	$C2/c$	corner- and edge-sharing	2.97
hmp	$(C_5H_{14}N_2)PbBr_4$	3D	$C2/m$	corner- and edge-sharing	3.04
hep	$(C_7H_{16}N)PbBr_3$	1D	Cc	face-sharing	3.50
hex	$(C_6H_{14}N)PbBr_3$	1D	$P2_1$	face-sharing	3.41

access a broader variety of white light-emitting materials.[35-39] In general, lower-dimensional structures possess more vibrational degrees of freedom and are more easily polarizable under photo-excitation, thus leading to enhancements in the STE process and to the amplification of the broad-band emission.[40-41]

Exploring the above concepts, we report here a variety of new hybrid lead bromide perovskites, representative of each kind, focusing on their white-light emission properties. We investigate the templating effect[42] of asymmetric diammonium organic cations based on the piperazinium and piperidinium backbone as seen in Figure 1a in the lead bromide system, since these types of cations are known to interact strongly with the anionic perovskite lattice.[18, 43] The resulting compounds present a library that includes 1D face-sharing structures, 1D corner- and edge-sharing structure, 2D (100)-oriented and (110)-oriented corner-sharing structures, to 3D corner- and edge-sharing structures as summarized in Table 1. We find that all the compounds reported here have broad-band PL emission at room temperature with different emission characteristics. We investigate the temperature-dependence of the PL emission and find the width of the broad-band emission for 2D and 3D structures becomes narrower when the temperature decreases, presumably due to deactivation of some STE states. The difference in the temperature dependence of the spectra with some displaying blue and others exhibiting red shifts, additionally suggests that different mechanisms are responsible for the different structure-types.

Notably, the 1D compound $(2,6\text{-dmpz})_3Pb_2Br_{10}$ stands out, having a PLQY of 12%, much higher than the rest of the examined compounds (<1%). The superior light emission properties of this 1D compound and the temperature evolution characteristics of the spectra provide new insights on structure-property relationships of halide perovskites and point to new design strategies (i.e. tuning the connectivity modes and dimensionality) towards white-light optoelectronic applications.

Results and discussion

Crystal structure

The hybrid lead bromide compounds presented here cover a wide variety of structural types in the perovskite family. Direct combination of the cation source in Figure 1a and $PbBr_2$ mixing in aqueous HBr at 122°C followed by slow-cooling of the solutions to room temperature yields colorless crystals, as seen in Figure 1b. Detailed synthesis procedures are listed in Methods section.

The 1D "perovskitoids"[44] (which refers to exclusively face-sharing ABX_3 compounds) (hep)$PbBr_3$ and (hex)$PbBr_3$ belong to the common $CsNiBr_3$ structure-type,[45] with face-sharing polymeric $[PbBr_3]^-$ chains (Figure 2). [46-54] Usually, a bulky cationic template, which is capable of separating the inorganic sections far apart, will lead to the formation of such low dimensional structure type.[44, 55] (hep)$PbBr_3$ and (hex)$PbBr_3$ crystallize in non-centrosymmetric monoclinic space groups Cc and $P2_1$, respectively. In Figure 2a, b, the infinite $[PbBr_3]^-$ chains in the structure extend along the c-axis for (hep)$PbBr_3$ (a-axis for (hex)$PbBr_3$), and the individual chains are crystallographically nonequivalent, which lower the symmetry. The monovalent organic cation rings are aligned parallel to the b-
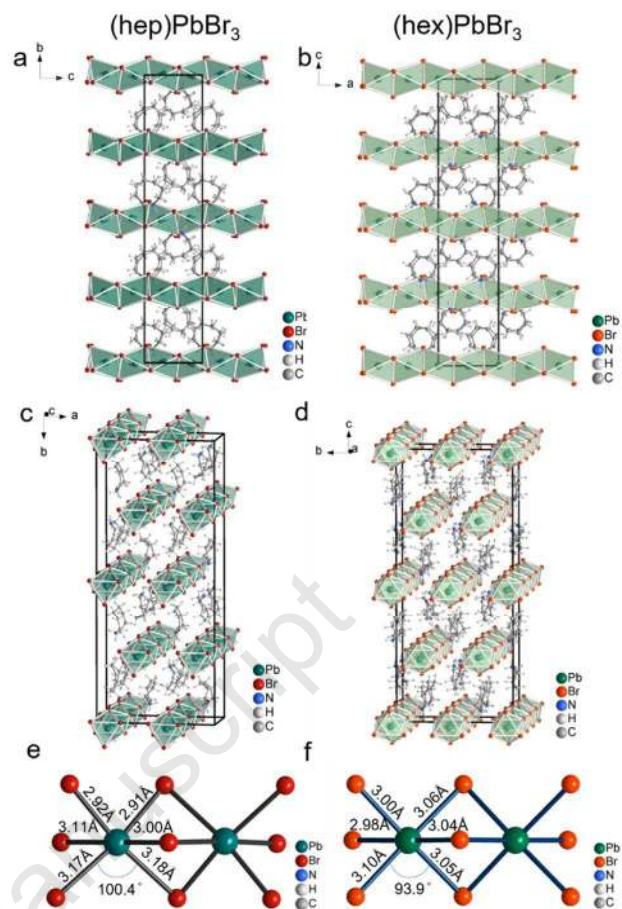

Figure 2. Crystal structures of (a), (c), (e) (hep)$PbBr_3$ and (b), (d), (f) (hex)$PbBr_3$. (a) and (b) show the side-view of the face-sharing 1D chains. In (e) and (f), it is clear that (hep)$PbBr_3$ has a more distorted structure than (hex)$PbBr_3$ (Br-Pb-Br angle 100.4˚ vs. 93.9˚, Pb-Br bond length 2.91 Å (shortest) and 3.18 Å (longest) vs. 2.98 Å (shortest) and 3.10 Å (longest).

axis for (hep)$PbBr_3$ (c-axis for (hex)$PbBr_3$), surrounding the inorganic chains. Due to the larger size of hep than hex, the lattice parameter along the longest axis of the unit cell increases from 37.860(2) Å for hex to 39.660(8) Å to hex. As shown in Figure 2e and 2f, the difference between the shortest and longest Pb-Br bond length is larger for (hep)$PbBr_3$ than that for (hex)$PbBr_3$ (2.91 Å and 3.18 Å vs. 2.98 Å and 3.10 Å). The Br-Pb-Br angles depicted in Figure 2e and 2f show a larger distortion for (hep)$PbBr_3$ (100.4˚) than that for

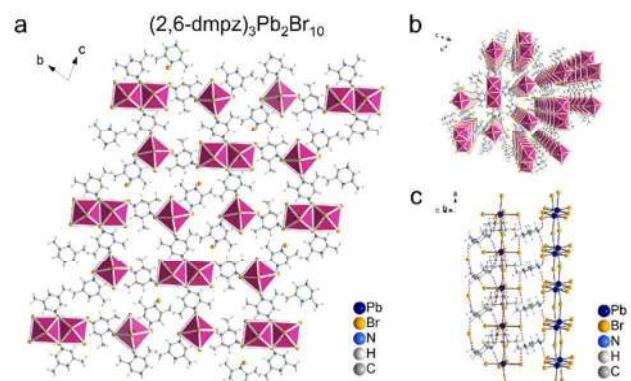**Figure 3.** Crystal structure of $(2,6\text{-dmpz})_3Pb_2Br_{10}$, which consists of two types of 1D chains as seen in (a) and (b). (c) Hydrogen bonding network associated with both chains.

3

(hex)PbBr$_3$ (93.9˚), with respect to a regular octahedron (90˚).

An exotic type of 1D structure combining edge- and corner-sharing double chains and single corner-sharing chains resulted from the use of the 2,6-dmpz cation (Figure 1a). Because of highly asymmetric unit, (2,6-dmpz)$_3$Pb$_2$Br$_{10}$ crystallizes in the triclinic space group *P*-1. The edge- and corner-sharing double anionic chain backbone has previously seen in (C$_{10}$H$_{12}$N$_2$)$_2$[Pb$_2$Br$_8$].[56] The hydrogen bonding pulls out a Br$^-$ anion from the perovskite lattice, in a similar fashion to the (en)$_2$PbBr$_6$ compound,[57] breaking the double-chain into a single corner-sharing chain and isolated Br$^-$ anions, which is shown in Figure 3a, making this structure unique. In Figure 3c, the discrete hydrogen bonding networks help to keep the continuity of the 1D single chains and double chains. The closest donor-acceptor distances (N-H$_{\cdots}$Br distance) occur with the isolated Br$^-$ and the cations, which are 3.28 Å and 3.29 Å.

(4amp)PbBr$_4$ and (epz)PbBr$_4$ represent (100)-oriented and (110)-oriented 2D perovskites, respectively, which are composed only of corner-sharing octahedra. The (110)-oriented type is much rarer as the corrugated layers are only able to form under specific hydrogen bonding interactions.[25, 29] The (100)-oriented 2D perovskite (4amp)PbBr$_4$ crystallizes in the non-centrosymmetric orthorhombic space group *Pca*2$_1$. The 4amp cations align in an unusual pattern, with the -CH$_2$NH$_3^+$ arms ordered in pairs, and with each pair arranged in an up-down configuration normal to the *ac*-plane (Figure 4a). The inorganic layers of (4amp)PbBr$_4$ exhibit large in-plane distortion, where the Pb-Br-Pb angle is 146˚, one of the smallest Pb-Br-Pb angles reported. The highly distorted layers are induced by strong hydrogen bonding, where the closest donor-acceptor
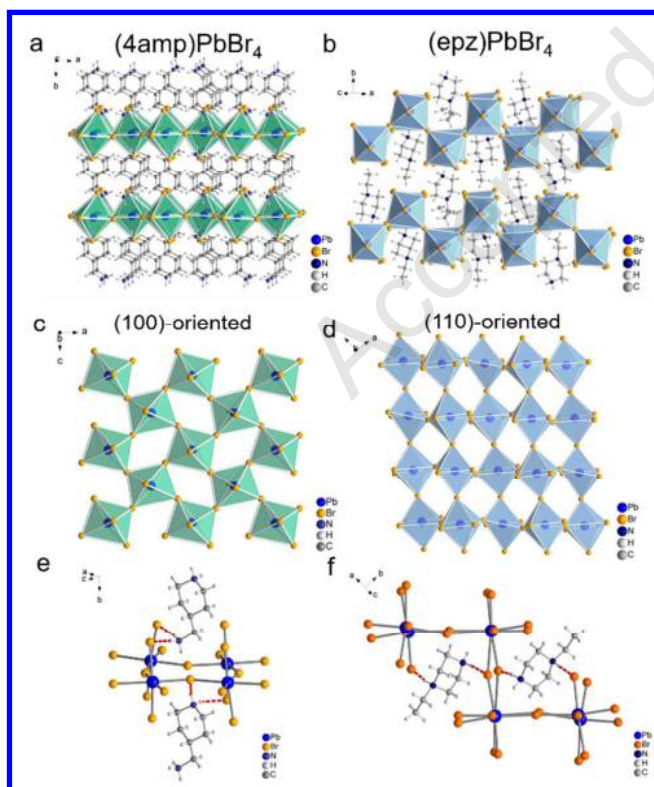

Figure 4. Crystal structures of (a), (c) and (e) (4amp)PbBr$_4$ and (b), (d) and (f) (epz)PbBr$_4$. (c), (d) Viewing perpendicular to the layers. (e), (f) Hydrogen bonds between the organic cations and inorganic layers.
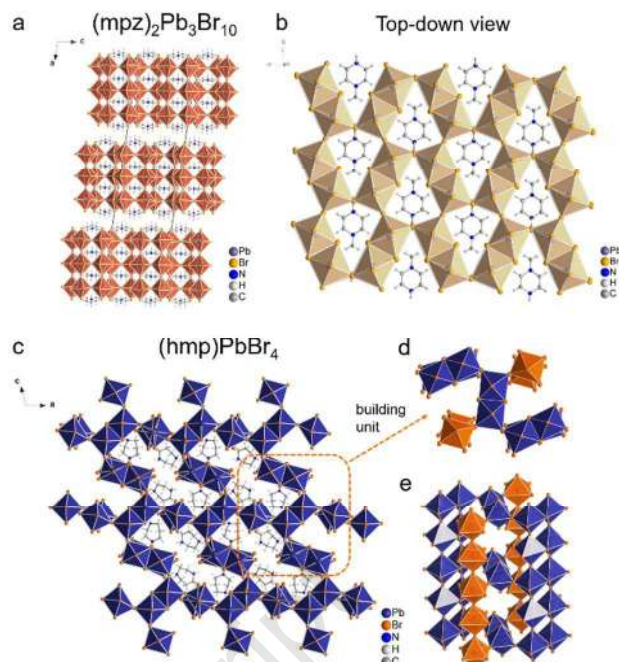

Figure 5. Crystal structures of (a) (mpz)$_2$Pb$_3$Br$_{10}$. (b) Top-down view of (mpz)$_2$Pb$_3$Br$_{10}$. Structure of (hmp)PbBr$_4$ (c, d and e). (d) and (e), basic building block of (hmp)PbBr$_4$.

distances are 3.33 Å and 3.35 Å.

(epz)PbBr$_4$ crystalizes in the non-centrosymmetric monoclinic space group *Pc*. The ability to stabilize a (110)-oriented 2D perovskite is closely related to the position of the protonation site of the organic spacer.[25-27] Here, the protonation of the cation happens at 1 and 4 positions on the aliphatic ring as seen in Figure 4f, which fits exactly in the perovskite pockets to form the hydrogen bonds (closest D-A distances: 3.23 Å and 3.24 Å). The use of piperazinium derivatives as organic cation yield the (110)-type as demonstrated in a (110)-oriented 2D structure (pipzH$_2$)[PbCl$_4$] which forms from the use of piperazinium as templates.[58]

Thicker layered 2D and 3D structures are also accessible from the use of asymmetric diammonium cations, with (mpz)$_2$Pb$_3$Br$_{10}$ (2D) and (hmp)PbBr$_4$ (3D) forming unique perovskite-related structure types. The crystal structures of (mpz)$_2$Pb$_3$Br$_{10}$ and (hmp)PbBr$_4$ are both centrosymmetric, crystallizing in the monoclinic space groups *C*2*/c* and *C*2*/m*, respectively. The unique three-layered structure of (mpz)$_2$Pb$_3$Br$_{10}$ is constructed from the basic building unit of edge-sharing [Pb$_2$Br$_{10}$]$^{6-}$, linked in a corner-sharing fashion to form ([Pb$_2$Br$_{10}$]$_4$) cages that encapsulate in-plane oriented mpz^{2+} cations (Figure 5a). The layer expansion is interrupted at the third layer, terminated by organic cations lying parallel to the layers. Similar organization of the inorganic layers and organic cations has been seen in C$_6$H$_9$N$_3$PbBr$_4$,[59] which is a single-layered perovskite constructed from ([Pb$_2$Br$_{10}$]$_4$) cages.

The 3D structure (hmp)PbBr$_4$ consists of similar building units as the 1D (2,6-dmpz)$_3$Pb$_2$Br$_{10}$, which are however connected in a different fashion. This structure represents a new structural type in the hybrid perovskite family. Rather than isolated 1D chains, the edge-sharing double chains (highlighted in blue, Figure 5d) and corner-sharing threads (highlighted in orange, Figure 5d) are linked to form the 3D framework.

4

Both the chains and the threads run down along the *b*-axis, and they are connected along the *ac*-plane through corner-sharing. The connectivity resembles the triangles seen in $(mpz)_2Pb_3Br_{10}$, but because of the linkage of asymmetric $[PbBr_5]^{3-}$ (corner-sharing) and $[Pb_2Br_{10}]^{6-}$ (edge-sharing) building blocks, as well as the larger ring size of hmp^{2+} over mpz^{2+} the triangles remain "open" (Figure 5e). Within the 3D framework, the extended cavities host the hmp^{2+} cations, with each thus formed channel filled with four organic cations. Although for the vast majority of cases, A_2PbX_4 compounds (A= organic cation) are 2D structures, the use of the relatively small size di-cation of hemp here seems to promote a new example of a $[PbX_4]^{2-}$ stoichiometry, that adopts a 3D rather that a 2D structure. This increase in dimensionality can rationalized by the so-called "counterion effect" which favors higher anion dimensionalities as the size of the counterion shrinks.[55]

a

b

Figure 6. (a) Low frequency Raman spectra of hybrid lead bromide crystals. The spectral region between ±15 cm^{-1} has been deleted because of the use of notch filter. (b) bond length distortion of bond angle variance of the compounds calculated based on the crystal structures.

Raman spectroscopy and structural distortion

To get a better picture of the local structural dynamics of the hybrid lead bromide perovskites, we performed low-frequency Raman measurements. The Raman spectra were obtained with 473 nm laser excitation in ambient condition. Unlike the 3D ABX$_3$-type perovskite CH$_3$NH$_3$PbBr$_3$ and CsPbBr$_3$ that exhibit broad un-resolved peaks at room temperature,[60] most of the compounds reported here have well-resolved spectra (Figure 6a). Depending on the dimensionality and connectivity mode of the crystal structure, the spectra show very different characteristics, consistent with the different connectivity modes of the $[PbBr_6]^{4-}$ octahedra. The peaks at lower wavenumbers (15-100 cm^{-1}) correspond to the bending of the Br-Pb-Br bonds, while the peaks at higher wavenumbers (100-180 cm^{-1}) originate from the stretching of the Pb-Br bonds, thus providing indirect information for the local environment of the compounds.[61-62]

For the face-sharing 1D compounds (hep)PbBr$_3$ and (hex)PbBr$_3$, the strong bonding pushes the symmetric mode to relatively high energy (142 cm^{-1}), and the rigidity of the face-sharing bonding increases the peak intensity. Edge- and corner-sharing compounds, by contrast, where the bonding becomes less rigid exhibit weak stretching modes. The other 1D compound, (2,6-dmpz)$_3$Pb$_2$Br$_{10}$, with corner- and edge-sharing connectivity shows many weak peaks with two pronounced symmetric modes at 135 cm^{-1} and 148 cm^{-1} likely corresponding to corner- and edge-sharing connectivity, respectively. The weak intensity and the diffuse underlying spectrum suggests the presence of anharmonicity in the structure, analogous to that observed for the MAPbBr$_3$ and CsPbBr$_3$ perovskites.[60]

The 2D compounds (4amp)PbBr$_4$, (epz)PbBr$_4$ and (mpz)$_2$Pb$_3$Br$_{10}$ all have strong Raman stretches at relatively low wavenumbers (~130 cm^{-1}), due to their strongly interconnected structures that promote concerted bending (octahedral tilting) than individual octahedral stretching. The 3D compound, (hmp)PbBr$_4$, has a less-resolved spectrum compared with other compounds, indicating a more dynamically disordered structure consistent with its higher dimensionality and its corner-sharing connectivity.[60]

Based on the refined crystal structures, we calculated the distortion levels of the individual $[PbBr_6]^{4-}$ octahedron for the individual compounds (Figure 6b). The bond length distortion[63-64] (eq.1, where *d* is the mean Pb-Br bond distance and d_n are the six individual Pb-Br bond distances) and bond angle variance[65] (eq.2, θi is the individual Pb-Br-Pb angle) reflect the deviation of the octahedron from the one with no distortion.

$$\Delta d = (\tfrac{1}{6})\Sigma \left[\frac{d_n - d}{d}\right]^2 \qquad (1)$$

$$\sigma^2 = \Sigma_{i=1}^{12}(\theta i - 90)^2 / 11 \qquad (2)$$

Previously, we have associated the distortion level of the 2D lead bromide perovskite with the width of the PL emission, where the larger the distortion, the broader the width of the PL emission.[25, 47] Although this correlation may apply to the 2D systems, it cannot be generalized to the 1D and 3D systems that have different connectivity modes. Here, we do not yet
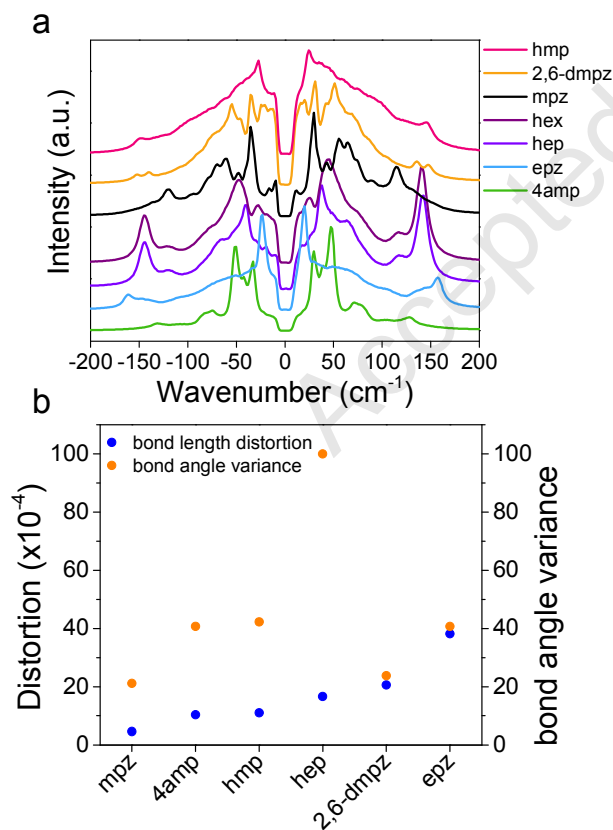
5

glean a correlation between the emission band width and the distortion level. However, most compounds display a large $PbBr_6$ distortion in the crystal structure. From the calculation, only $(mpz)_2Pb_3Br_{10}$ has a relatively small distortion level for both the angular and bond length distortion. The highest bond length distortion in observed in (110)-oriented 2D perovskite $(epz)PbBr_4$. For the angular distortion, $(hep)PbBr_3$ has the highest due to the face-sharing connectivity of the octahedron that requires bent angles (i.e. Br-Pb-Br angle). In general, the high distortion level of the local octahedral environments implies a more malleable structure which is more susceptible to generating STE states upon photo-excitation, thus producing a broad-band emission spectrum.

Electronic structure calculations

To further understand the electronic properties of these materials, we use density functional theory (DFT) for the calculation of the band structures. Because of the presence of heavy elements, spin-orbit coupling was taken into account. We chose two 1D structures and two 2D structures as representative examples to distinguish the effect of dimensionality and
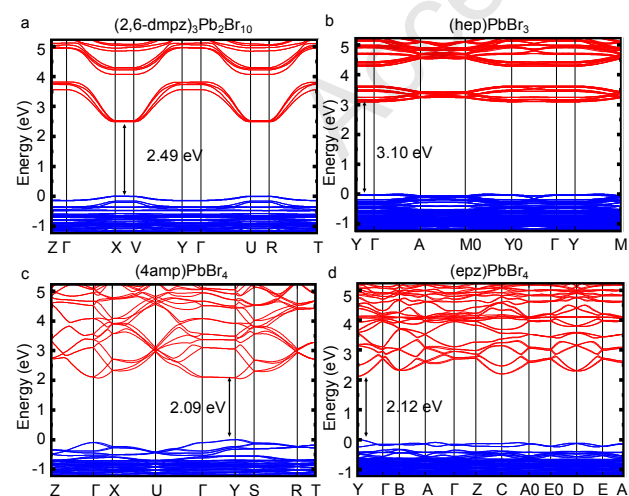
Figure 7. Calculated electronic band structures of (a) $(2,6\text{-}dmpz)_3Pb_2Br_{10}$ (2.49 eV), (b) $(hep)PbBr_3$ (3.10 eV), (c) $(4amp)PbBr_4$ (2.09 eV) and (d) $(epz)PbBr_4$ (2.12 eV).

connectivity on the band gap. Notice that dimensionality is defined in the present manuscript by the nature of the bonding

network. $(2,6\text{-}dmpz)_3Pb_2Br_{10}$ is referred in the text as a 1D material for this reason. The band dispersion diagram in Figure 7a reveals flat electronic dispersions close to the band gap along both X-V and U-R directions. $(2,6\text{-}dmpz)_3Pb_2Br_{10}$ can thus also be considered as an array of quantum wires along the ox direction. The 2D materials $(4amp)PbBr_4$ and $(epz)PbBr_4$ can thus be considered as quantum well superlattices with the same criterion (Figures 7c and 7d). Comparison among the 1D structures $(2,6\text{-}dmpz)_3Pb_2Br_{10}$ and $(hep)PbBr_3$ reveals that the former (the 1D material with edge- and corner-sharing) has much more dispersive bands and smaller band gap (2.49 eV) than the latter (1D face-sharing), which has flat bands and much larger band gap (3.10 eV), clearly illustrating that the connectivity of the octahedra is detrimental to the electronic structure. Mixed corner- and edge-sharing affords significantly more dispersion than face-sharing connectivity, especially for the CBM states.

The difference in the band structure for the (100)-oriented and (110)-oriented 2D structures are not very significant in Figure 7c and 7d, which the (100)-oriented $(4amp)PbBr_4$ has a slightly smaller band gap (2.09 eV) than the (110)-oriented $(epz)PbBr_4$ (2.12 eV), consistent with the experiment. Both compounds have similar dispersion for both the valence and conduction bands. Note that the calculated band gaps are underestimated but still follow the same trend with respect to the experimental result, as shown in Figure S2. All compounds are

Figure 8. (a) Experimental energy band alignment of hybrid lead bromide compounds. VBM and CBM of the various compounds compared with the 3D $MAPbBr_3$ perovskite and $PbBr_2$. (b) Optical absorption spectra of the compounds reported here. Detailed values are listed in Table 1. Steady-state PL (excited at 330 nm) at room temperature for (c) $(hmp)PbBr_4$, $(2,6\text{-}dmpz)_3Pb_2Br_{10}$ and $(mpz)_2Pb_3Br_{10}$, (d) $(hep)PbBr_3$ and $(hex)PbBr_3$, (e) $(4amp)PbBr_4$ and $(epz)PbBr_4$.

6

direct gap semiconductors, with the valence band maximum (VBM) composed of hybridization of Br p and Pb s orbitals and conduction band minimum (CBM) composed of empty Pb p orbitals as seen in the corresponding pDOS in Figure S3.

Optical properties

Because the new perovskite compounds could potentially be used in future devices it is of fundamental importance to have knowledge of the energy positions of their valence and conduction bands and to understand the trends with which they vary from one member to the next. Experimental determination of such energy values in most perovskites are rare and often frustrate device design in terms of the correct design of interface assembly. Therefore, valance band maxima (VBM), of the different compounds were measured by ambient photoemission spectroscopy (APS) (Figure 8a). The conduction band minima (CBM) were calculated by adding the band gap energy, measured by diffuse reflectance spectroscopy in Figure 8b. We cluster the compounds according to their octahedra connectivity modes. The samples with both corner- and edge-sharing octahedra (2,6-dmpz, hmp, mpz), show variation in their VBM, while their CBM is almost constant. In contrary, the compounds with corner-sharing (epz, 4amp), or face-sharing (hep, hex), octahedra has strong variation of the CBM while the VBM remains almost constant.

The optical properties of these materials are dominated by the connectivity mode of the $[PbBr_6]^{4-}$ octahedra, where the band gap follow the general trend of "corner-sharing< edge-sharing< face-sharing", as expected from the corresponding Pb-Br orbital overlap. The same trend has been observed in the lead iodide system.[66] Specifically, for the corner-connected compounds, $(4amp)PbBr_4$ consists of only corner-sharing octahedra and has the smallest band gap (2.93 eV) in the series (see Figure 8b). This bandgap is slightly larger than some other (100)-oriented 2D perovskites, such as $(DMAPA)PbBr_4$ (2.88 eV) and $(DMABA)PbBr_4$ (2.85 eV) because of its sizeable in-plane distortions.[29] The (110)-oriented 2D perovskite $(epz)PbBr_4$ has a larger bang gap of 3.12 eV because of the highly corrugated character of the layer.

The compounds possessing both corner- and edge- sharing octahedra (mpz, hmp and 2,6-dmpz) have larger band gaps 2.97 eV, 3.04 eV and 3.16 eV, respectively than the purely corner-sharing $(4amp)PbBr_4$. As mentioned earlier, the compounds (hep and hex) with face-sharing octahedra have the largest band gap of 3.41 eV and 3.50 eV. For the 1D face-sharing structures, $(hep)PbBr_3$ has a slightly larger band gap than $(hex)PbBr_3$ as the 1D chains are more distorted as described above.

Despite that the optical spectra show sharp absorption edge, the PL spectra of all compounds exhibit broad band emission features at room temperature. Except for $(hep)PbBr_3$ and $(hex)PbBr_3$ which emit in the red, the rest of the compounds emit white-light with different emission width and peak position. In the following discussion, we group the PL emission of these compounds based on the connectivity mode as seen in Table 1. The centers of the PL emission for $(mpz)_2Pb_3Br_{10}$ (2.20 eV), $(hmp)PbBr_4$ (2.04 eV) and $(2,6\text{-}dmpz)_3Pb_2Br_{10}$ (2.12 eV) are relatively close together (Figure 8b). In addition to the broad emission peak at 2.04 eV, $(hmp)PbBr_4$ has another well-resolved higher energy emission peak at 2.81 eV. For $(hep)PbBr_3$ and $(hex)PbBr_3$ the emissions are very similar, Figure 8c. Both 1D face-sharing compounds have a weak high energy emission peak at ~2.75 eV and the main emission peak at ~1.84 eV. The main emission peak of $(hep)PbBr3$ at 1.84 eV is far away from the absorption edge at 3.5 eV, demonstrating a large Stokes shift of 1.66 eV. Compounds such as $(tms)_4Pb_3Br_{10},$[67] and $(C_6H_{14}N)PbBr_3,$[68] which are also partially composed of face-sharing components, have similar emission characteristics, in the sense that there is a huge Stokes shift and the emission starting around 3 eV and peaking at 1.77-1.90 eV. Compared to (100)-oriented $(4amp)PbBr_4$, the (110)-oriented $(epz)PbBr_4$ has a more red-shifted peak emission (2.08 eV), but the emission center for $(4amp)PbBr_4$ occurs at lower wavelength (2.38 eV), Figure 8e. Except for $(hmp)PbBr_4$ which as a shoulder peak at higher energy, all compounds fit the trend where the larger the band gap, the more red-shifted the center of the emission peak is.

Among all compounds, $(2,6\text{-}dmpz)_3Pb_2Br_{10}$ has a PLQY of 12%, which is much higher than the rest (<1%, see Table 2). It
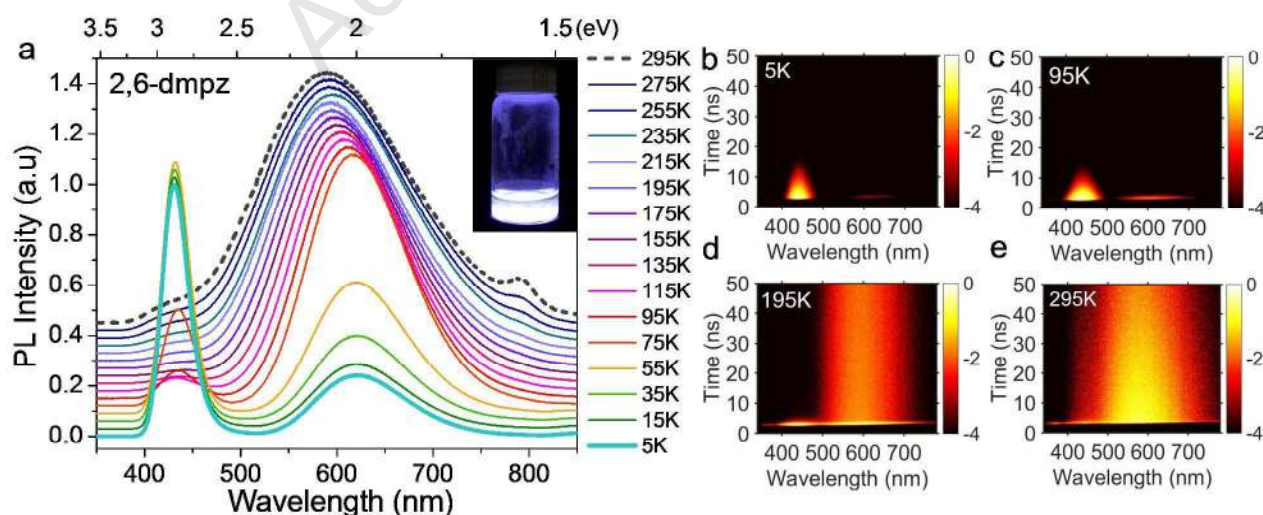

Figure 9. (a) Temperature-dependent (5 – 293 K) steady-state PL spectra of $(2,6\text{-}dmpz)_3Pb_2Br_{10}$. Inserted shows the sample emitting white-light under UV flashlight. (b)-(e) 2D TRPL of $(2,6\text{-}dmpz)_3Pb_2Br_{10}$ at various temperatures; the colorbar shown on the right of each 2D plot is in log10 scale.

is also among the highest PLQY reported for hybrid perovskite white-light emitting materials.[31] The reason for the high PLQY may be attributed to the unique mixed 1D edge-sharing and corner-sharing structure, which shares some similarities with the 1D edge-sharing compound $C_4N_2H_{14}PbBr_4$ that demonstrates a high PLQY of 20%.[31]

To investigate the mechanistic aspects of the broad-band emission, we performed variable-temperature PL. The temperature-dependent PL measurement of $(2,6\text{-dmpz})_3Pb_2Br_{10}$ shows the unusual evolution of the PL emission from 295K to 5K in Figure 9. At 293K, the PL emission is a broad peak from 400 nm to 750 nm (1.65-3.1 eV), centered at 585 nm (2.12 eV). Upon decreasing the temperature, the broad peak starts to become narrower and shifts to longer wavelengths (from 585 nm at 295K to 620 nm at 5K). A new higher energy peak then appears at 115 K, centered at 432 nm (2.87 eV). The two distinct peaks have different intensities and decay lifetimes as seen in Figure 9b-e.

For $(2,6\text{-dmpz})_3Pb_2Br_{10}$, the averaged lifetime of the broad emission peak at 295K is 23.03 ns, which is the longest among all the compounds reported here. The rest of the compounds have much shorter PL lifetimes ranging from 2-4 ns (Table 2, Figure S9), which are comparable to previously reported hybrid lead bromide perovskites.[29] At 195K, the lifetime of the emission of $(2,6\text{-dmpz})_3Pb_2Br_{10}$ at ~600 nm (2.07 eV) is 28.02 ns, whereas the lifetime of the emission at ~450 nm (2.76 eV) is 0.56 ns. The lifetime of the emission at ~600 nm (2.07 eV) becomes increasingly shorter as the temperature decreases, where it reaches the shortest (0.78 ns) at 5K in Figure 9b, whereas the lifetime of the emission at ~450 nm increases to 2.95 ns. Intensity-wise, the peak at ~600 nm reaches its maximum at 235K (Figure S8) and decreases to its minimum value at 5K. The emission at ~450 compound $(2,6\text{-dmpz})_3Pb_2Br_{10}$ nm on the other hand, reaches the maximum intensity value at 15K.

The trend of the temperature dependence for the 2D and 3D compounds can be generally summarized as the bandwidth of the PL broadband emission peak gradually decreasing as the temperature lowers as shown in Figure 10. For example, the full-width at half-maximum (FWHM) of the (100)-oriented 2D compound $(4amp)PbBr_4$ decreases from 420 meV (295K)

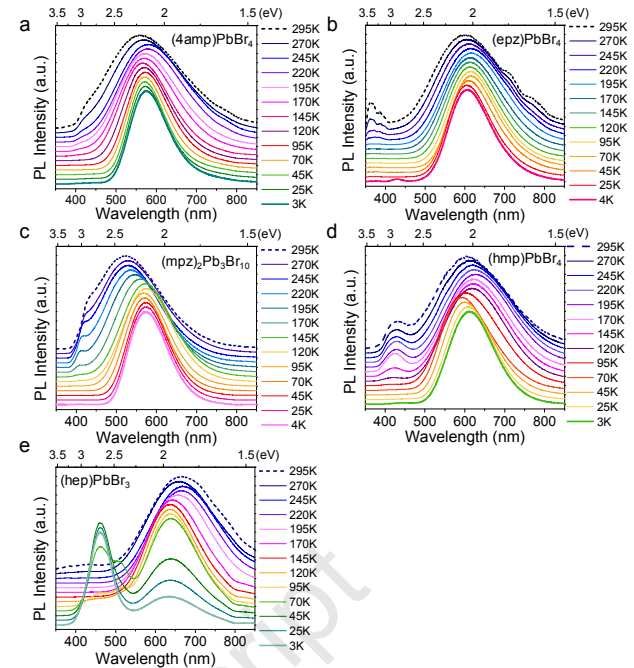to 210 meV (5K). $(epz)PbBr_4$, $(mpz)_2Pb_3Br_{10}$ and $(hmp)PbBr_4$

Figure 10. Temperature-dependent (3 – 295 K) steady-state PL spectra (normalized intensity) of (a)$(4amp)PbBr_4$, (b) $(epz)PbBr_4$, (c) $(mpz)_2Pb_3Br_{10}$, (d)$(hmp)PbBr_4$, (e) $(hep)PbBr_3$.

have shown the same tendency where their emission bandwidth also decreases in Figure 10b, c and d, respectively.

Unlike the higher dimensional compounds, the 1D compound $(hep)PbBr_3$, has similar emission characteristics as the 1D compound $(2,6\text{-dmpz})_3Pb_2Br_{10}$ discussed earlier, where the broad peak at 669 nm (1.85 eV) gradually narrows while another high energy peak at ~460 nm (2.70 eV) surfaces at around 145K. A reported 1D face-sharing compound, [1,5-Bis(1-methylimidazolium)pentane][PbBr$_3$]$_2$, has almost the exact same PL evolution from RT to 10K,[47] suggesting this trend is dimension-dependent.

Upon cooling the width of the PL emission becomes narrower. The different modes of the PL evolution suggest there are several energy transfer processes happening when decreas-

Table 2. Commission International de l'Eclairage (CIE) coordinates (x, y), correlated color temperature (CCT), color rendering index (CRI), PL emission center, PL lifetime at room temperature, full-width at half-maximum (FWHM) and photoluminescence quantum yield (PLQY) of the new compounds reported here.

Compound	x	y	CCT	CRI	PL emission center (eV)	τ_{avg} (ns)	FWHM (meV)	PLQY (%)
2,6-dmpz	0.44	0.46	3341	77	2.12	23.03	325	12.24
epz	0.44	0.44	3324	84	2.08	2.7	370	0.97
mpz	0.38	0.42	4242	86	2.20	3.6	485	0.33
hmp	0.41	0.39	3379	90	2.04	2.5	570	0.46
hep	0.52	0.41	1986	89	1.84	4.3	285	0.63
hex	0.54	0.40	1801	88	1.82	NA	270	0.35
4amp	0.31	0.39	6275	76	2.38	2.5	420	0.54

ing the temperature, where the thermally activated processes are less pronounced and locally confined. Usually at sufficiently low temperature, (the lowest we can measure is 3~5K), the free exciton PL, as compared to self-trapped excitons, should be dominant (higher energy emission, ~450 nm (2.76 eV)). Here we see for 4amp, epz, mpz and hmp the STE emission (~450 nm, 2.75 eV) still dominates the overall emission, suggesting the highly distorted structures prevent the STEs from tunneling back to the free exciton states. Finally, for the 1D structure (hep)PbBr$_3$ in Figure 10e, the free exciton emission at higher energy is dominant over the suppressed broad STE states at low temperature (3- 45K), which is similar to the other 1D compound (2,6-dmpz)$_3$Pb$_2$Br$_{10}$.

White-light emission

2,6-dmpz)$_3$Pb$_2$Br$_{10}$, (4amp)PbBr$_4$, (epz)PbBr$_4$, (mpz)$_2$Pb$_3$Br$_{10}$ and (hmp)PbBr$_4$ have relatively warm white-light emission as shown in Figure 11 compared to our previously investigated systems α-(DMEN)PbBr$_4$[29] and EA$_4$Pb$_3$Br$_{10-x}$Cl$_x$.[69] The correlated color temperature (CCT) of most compounds are below 4500K (except (4amp)PbBr$_4$, 6275K), producing neutral to warm white-light. The color rendering index (CRI) are quite high (above 85, see Table 2) for most compounds, providing accurate color rendition of the actual objects. (2,6-dmpz)$_3$Pb$_2$Br$_{10}$ has a CIE coordinate of (0.44, 0.46) which has a reddish white-emission comparing to the white point at (0.33, 0.33). Although (2,6-dmpz)$_3$Pb$_2$Br$_{10}$ has the highest PLQY, and better potential of actual application in solid-state lighting,[35] the CRI (77) is lower than most of the compounds reported here. This could be improved by using halide-mixing strategy as shown in earlier reports.[69]

Conclusions

Seven new hybrid lead bromide compounds, namely (hep)PbBr$_3$, (hex)PbBr$_3$, (2,6-dmpz)$_3$Pb$_2$Br$_{10}$, (4amp)PbBr$_4$, (epz)PbBr$_4$, (mpz)$_2$Pb$_3$Br$_{10}$ and (hmp)PbBr$_4$, perovskites and perovskitoids possess a diverse range of structural types with
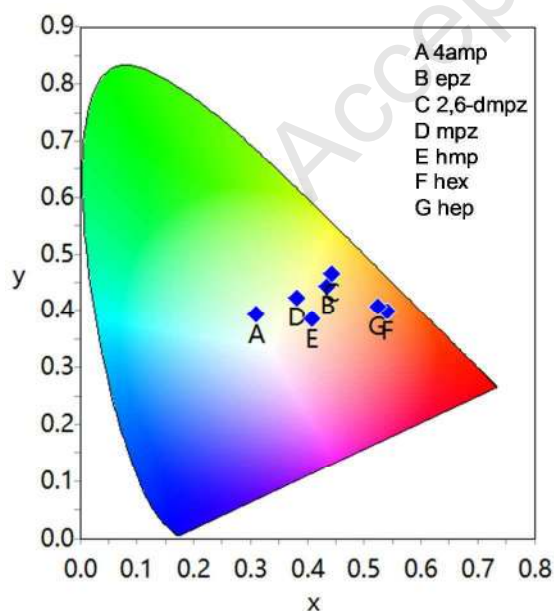

Figure 11. CIE color coordinates of the hybrid lead bromide compounds in 1931 color space chromaticity diagram. The chromaticity coordinates (x, y), CCT and CRI are calculated using the ColorCalculator by OSRAM Sylvania, Inc.

different octahedral connectivity. The connectivity modes of the [PbBr$_6$]$^{4-}$ octahedra determine the optical band gaps of these materials in a "corner-sharing< edge-sharing< face-sharing" increasing order. Except for the face-sharing (hep)PbBr$_3$ and (hex)PbBr$_3$, the rest of the compounds exhibit white-light emission at room temperature (RT). Temperature-dependent PL studies have revealed that for 1D compounds a prominent peak at higher energy emerges (free exciton dominates at low temperature) while for 2D and 3D compounds the broad emission peak gradually becomes narrower when decreasing the temperature (STE dominates). The unique 1D compound (2,6-dmpz)$_3$Pb$_2$Br$_{10}$ which has a structure that combines corner- and edge-sharing octahedra has the highest PLQY (12%) and longest lifetime (23.03 ns) among them, while the remaining compounds have low PLQY (<1%) and relatively short lifetime (<5 ns). The diversity of the hybrid bromide perovskite as epitomized by the structural types reported here, enriches the expanding hybrid perovskite library. The superior PL properties of the 1D compound demonstrate that dimensional reduction to 1D perovskites can underpin a new direction for exploring suitable candidates for white-light solid-state lighting and other optoelectronic phenomena.

Methods

Materials. PbBr$_2$ (98%),1-methylpiperazine (99%), 1-ethylpiperazine (98%), 4-(aminomethyl)piperidine (96%), 2,6-dimethylpiperazine (97%) , homopiperazine (98%), hexamethyleneimine (98%) , heptamethyleneimine (98%), hydrobromic acid (ACS reagent, 48%) were purchased from Sigma-Aldrich and used as received.

Synthesis. The following procedure was used for the syntheses of all compounds. An amount of 1.10 g (3 mmol) of PbBr$_2$ was dissolved in 4 ml HBr under heating and stirring at 122 °C (A). 1 ml HBr was added into a separate vial of 3 mmol of 4-(aminomethyl)piperidine (B). The protonated 4-(aminomethyl)piperidine solution was added into A under heating for 2 min and cooled to room temperature. Plate-like crystals precipitate during slow-cooling. Yield 726 mg, (37.8% based on Pb content). The cation input varies for the rest of the compound while PbBr$_2$ stays constant: 1-methylpiperazine (200 mg, 2 mmol), 1-ethylpiperazine (342 mg, 3 mmol), 2,6-dimethylpiperazine (342 mg, 3 mmol), homopiperazine (300 mg, 3 mmol), hexamethyleneimine (297 mg, 3 mmol) and heptamethyleneimine (339 mg, 3 mmol).

Single Crystal X-ray Diffraction. Full sphere data were collected after screening for ten frames using either a STOE IPDS 2 or IPDS 2T diffractometer with graphite-monochromatized Mo Kα radiation (λ = 0.71073 Å) (50 kV/40 mA) under N$_2$ at 293K((4amp)PbBr$_4$, (epz)PbBr$_4$, (hep)PbBr$_3$, (mpz)$_2$Pb$_3$Br$_{10}$ and (hmp)PbBr$_4$). The collected data was integrated and applied with numerical absorption corrections using the STOE X-AREA programs. The rest of the compounds were collected either using a Bruker DUO or Molly instrument with MoKα IμS microfocus source (λ = 0.71073 Å) with MX Optics at 250K. The collected data was integrated and applied with numerical absorption corrections using the APEX3 software. Crystal structures were solved by direct methods and refined by full-matrix least-squares on F^2 using the OLEX2 program package.[70]

Optical Absorption Spectroscopy. Optical diffuse reflectance measurements were performed using a Shimadzu UV-

9

3600 UV-VIS-NIR spectrometer operating in the 200–1000 nm region using $BaSO_4$ as the reference of 100% reflectance. The band gap of the material was estimated by converting reflectance to absorption according to the Kubelka–Munk equation: $\alpha/S = (1-R)^2(2R)^{-1}$, where R is the reflectance and α and S are the absorption and scattering coefficients, respectively.[71]

Steady State and Time-resolved Photoluminescence. The samples were excited with 330 nm photons produced from an optical parametric amplifier, which is pumped by a titanium: sapphire amplifier with 800-nm output at 2-kHz repetition rate. Time-integrated photoluminescence (PL) spectra were captured with a CCD camera; time-resolved PL spectra were captured with a streak camera. During the measurements, the samples were mounted in a vacuum cryostat and maintained under $<10^{-7}$ Torr pressure. Quantum yield measurements were performed with a Horiba Jobin-Yvon Nanolog Spectrofluorimeter equipped with an integrating sphere. The samples were measured in powder form following an earlier report. [72]

Electronic Structure Calculations. First-principles calculations are based on density functional theory (DFT) as implemented in the SIESTA package.[73-74] Calculations have been carried out on experimental structures with the GGA functional in the revPBE form.[75] Core electrons are described with Troullier-Martins pseudopotentials.[76] The valence wavefunctions are developed over double-ζ polarized basis set of finite-range numerical pseudoatomic orbitals.[77] In our calculations, spin-orbit coupling is taken into account through the on-site approximation as proposed by Fernández-Seivane et al.[78] In all cases, an energy cutoff of 150 Ry for real-space mesh size has been used.

Supporting Information

X-ray crystallographic data for (hep)PbBr₃, (hex)PbBr₃, (2,6-dmpz)₃Pb₂Br₁₀, (4amp)PbBr₄, (epz)PbBr₄, (mpz)₂Pb₃Br₁₀ and (hmp)PbBr₄ (CIF), calculated and experimental powder X-ray diffraction patterns, additional calculation and PL data (PDF). This material is available free of charge via the Internet at http://pubs.acs.org.

Corresponding Author

*m-kanatzidis@northwestern.edu
*konstantinos.stoumpos@northwestern.edu

REFERENCES

1. Saparov, B.; Mitzi, D. B., *Chem. Rev.* **2016,** *116*, 4558-4596.
2. Stoumpos, C. C.; Kanatzidis, M. G., *Acc. Chem. Res.* **2015,** *48*, 2791-2802.
3. Snaith, H. J., *J. phys. Chem. Lett.* **2013,** *4*, 3623-3630.
4. Wang, N.; Liu, W.; Zhang, Q., *Small Methods* **2018,** *2*, 1700380.
5. Ning, C.-Z.; Dou, L.; Yang, P., *Nat. Rev. Mater.* **2017,** *2*, 17070.
6. Shi, E.; Gao, Y.; Finkenauer, B. P.; Akriti; Coffey, A. H.; Dou, L., *Chem. Soc. Rev.* **2018,** *47*, 6046-6072
7. Correa-Baena, J.-P.; Saliba, M.; Buonassisi, T.; Grätzel, M.; Abate, A.; Tress, W.; Hagfeldt, A., *Science* **2017,** *358*, 739-744.
8. Wang, N.; Zhao, K.; Ding, T.; Liu, W.; Ahmed, A. S.; Wang, Z.; Tian, M.; Sun, X. W.; Zhang, Q., *Advanced Energy Materials* **2017,** *7*, 1700522.
9. Kojima, A.; Teshima, K.; Shirai, Y.; Miyasaka, T., *J. Am. Chem. Soc.* **2009,** *131*, 6050-6051.
10. Yang, W. S.; Park, B.-W.; Jung, E. H.; Jeon, N. J.; Kim, Y. C.; Lee, D. U.; Shin, S. S.; Seo, J.; Kim, E. K.; Noh, J. H.; Seok, S. I., *Science* **2017,** *356*, 1376-1379.
11. Gu, P.-Y.; Wang, N.; Wang, C.; Zhou, Y.; Long, G.; Tian, M.; Chen, W.; Sun, X. W.; Kanatzidis, M. G.; Zhang, Q., *Journal of Materials Chemistry A* **2017,** *5*, 7339-7344.
12. Stranks, S. D.; Snaith, H. J., *Nat. Nanotechnol.* **2015,** *10*, 391-402.
13. Wang, N.; Cheng, L.; Ge, R.; Zhang, S.; Miao, Y.; Zou, W.; Yi, C.; Sun, Y.; Cao, Y.; Yang, R.; Wei, Y.; Guo, Q.; Ke, Y.; Yu, M.; Jin, Y.; Liu, Y.; Ding, Q.; Di, D.; Yang, L.; Xing, G.; Tian, H.; Jin, C.; Gao, F.; Friend, R. H.; Wang, J.; Huang, W., *Nat. Photon.* **2016,** *10*, 699–704
14. Yuan, M.; Quan, L. N.; Comin, R.; Walters, G.; Sabatini, R.; Voznyy, O.; Hoogland, S.; Zhao, Y.; Beauregard, E. M.; Kanjanaboos, P.; Lu, Z.; Kim, D. H.; Sargent, E. H., *Nat. Nanotechnol.* **2016,** *11*, 872-877.
15. Tsai, H.; Nie, W.; Blancon, J. C.; Stoumpos, C. C.; Soe, C. M. M.; Yoo, J.; Crochet, J.; Tretiak, S.; Even, J.; Sadhanala, A., *Adv. Mater.* **2018,** *30*, 1704217.
16. Stoumpos, C. C.; Malliakas, C. D.; Kanatzidis, M. G., *Inorg. Chem.* **2013,** *52*, 9019-9038.
17. Stoumpos, C. C.; Cao, D. H.; Clark, D. J.; Young, J.; Rondinelli, J. M.; Jang, J. I.; Hupp, J. T.; Kanatzidis, M. G., *Chem. Mater.* **2016,** *28*, 2852-2867.
18. Mao, L.; Ke, W.; Pedesseau, L.; Wu, Y.; Katan, C.; Even, J.; Wasielewski, M. R.; Stoumpos, C. C.; Kanatzidis, M. G., *J. Am. Chem. Soc.* **2018,** *140*, 3775-3783.
19. Sun, C.; Wang, M. S.; Li, P. X.; Guo, G. C., *Angewandte Chemie International Edition* **2017,** *56*, 554-558.
20. Lee, B.; Stoumpos, C. C.; Zhou, N.; Hao, F.; Malliakas, C.; Yeh, C.-Y.; Marks, T. J.; Kanatzidis, M. G.; Chang, R. P. H., *J. Am. Chem. Soc.* **2014,** *136*, 15379-15385.

21. Saidaminov, M. I.; Almutlaq, J.; Sarmah, S.; Dursun, I.; Zhumekenov, A. A.; Begum, R.; Pan, J.; Cho, N.; Mohammed, O. F.; Bakr, O. M., *ACS Energy Lett.* **2016,** *1*, 840-845.

22. De Bastiani, M.; Dursun, I.; Zhang, Y.; Alshankiti, B. A.; Miao, X.-H.; Yin, J.; Yengel, E.; Alarousu, E.; Turedi, B.; Almutlaq, J. M.; Saidaminov, M. I.; Mitra, S.; Gereige, I.; AlSaggaf, A.; Zhu, Y.; Han, Y.; Roqan, I. S.; Bredas, J.-L.; Mohammed, O. F.; Bakr, O. M., *Chem.Mater.* **2017,** *29*, 7108-7113.

23. Tran, T. T.; Panella, J. R.; Chamorro, J. R.; Morey, J. R.; McQueen, T. M., *Mater.Horiz.* **2017,** *4*, 688-693.

24. Smith, M. D.; Karunadasa, H. I., *Acc. Chem. Res.* **2018,** *51*, 619-627.

25. Li, Y. Y.; Lin, C. K.; Zheng, G. L.; Cheng, Z. Y.; You, H.; Wang, W. D.; Lin, J., *Chem. Mater.* **2006,** *18*, 3463-3469.

26. Dohner, E. R.; Hoke, E. T.; Karunadasa, H. I., *J. Am. Chem. Soc.* **2014,** *136*, 1718-1721.

27. Dohner, E. R.; Jaffe, A.; Bradshaw, L. R.; Karunadasa, H. I., *J. Am. Chem. Soc.* **2014,** *136*, 13154-13157.

28. Hu, T.; Smith, M. D.; Dohner, E. R.; Sher, M.-J.; Wu, X.; Trinh, M. T.; Fisher, A.; Corbett, J.; Zhu, X. Y.; Karunadasa, H. I.; Lindenberg, A. M., *J. Phys. Chem. Lett.* **2016,** *7*, 2258-2263.

29. Mao, L.; Wu, Y.; Stoumpos, C. C.; Wasielewski, M. R.; Kanatzidis, M. G., *J. Am. Chem. Soc.* **2017,** *139*, 5210–5215.

30. Cortecchia, D.; Neutzner, S.; Srimath Kandada, A. R.; Mosconi, E.; Meggiolaro, D.; De Angelis, F.; Soci, C.; Petrozza, A., *J. Am. Chem. Soc.* **2017,** *139*, 39-42.

31. Yuan, Z.; Zhou, C.; Tian, Y.; Shu, Y.; Messier, J.; Wang, J. C.; Van De Burgt, L. J.; Kountouriotis, K.; Xin, Y.; Holt, E., *Nat. Commun.* **2017,** *8*, 14051.

32. Mercier, N.; Louvain, N.; Bi, W., *CrystEngComm* **2009,** *11*, 720-734.

33. Long, J. R.; McCarty, L. S.; Holm, R., *J. Am. Chem. Soc.* **1996,** *118*, 4603-4616.

34. Axtell III, E. A.; Liao, J. H.; Pikramenou, Z.; Kanatzidis, M. G., *Chem.Eur. J.* **1996,** *2*, 656-666.

35. Wang, M.-S.; Guo, G.-C., *Chem. Commun.* **2016,** *52*, 13194-13204.

36. Wang, M.-S.; Guo, S.-P.; Li, Y.; Cai, L.-Z.; Zou, J.-P.; Xu, G.; Zhou, W.-W.; Zheng, F.-K.; Guo, G.-C., *J. Am. Chem. Soc.* **2009,** *131*, 13572-13573.

37. Wang, M. S.; Guo, G. C.; Chen, W. T.; Xu, G.; Zhou, W. W.; Wu, K. J.; Huang, J. S., *Angew. Chem. Int. Ed.* **2007,** *46*, 3909-3911.

38. Wang, G.-E.; Xu, G.; Wang, M.-S.; Cai, L.-Z.; Li, W.-H.; Guo, G.-C., *Chem. Sci.* **2015,** *6*, 7222-7226.

39. Sun, C.; Xu, G.; Jiang, X.-M.; Wang, G.-E.; Guo, P.-Y.; Wang, M.-S.; Guo, G.-C., *J. Am. Chem. Soc.* **2018,** *140*, 2805-2811.

40. Saidaminov, M. I.; Mohammed, O. F.; Bakr, O. M., *ACS Energy Lett.* **2017,** *2*, 889–896.

41. Lin, H.; Zhou, C.; Tian, Y.; Siegrist, T.; Ma, B., *ACS Energy Lett.* **2018,** *3*, 54-62.

42. Zhang, Z.-J.; Guo, G.-C.; Xu, G.; Fu, M.-L.; Zou, J.-P.; Huang, J.-S., *Inorg. Chem.* **2006,** *45*, 10028-10030.

43. Li, M.-Q.; Hu, Y.-Q.; Bi, L.-Y.; Zhang, H.-L.; Wang, Y.; Zheng, Y.-Z., *Chem.Mater.* **2017,** *29*, 5463-5467.

44. Stoumpos, C. C.; Mao, L.; Malliakas, C. D.; Kanatzidis, M. G., *Inorg. Chem.* **2017,** *56*, 56-73.

45. Raw, A. D.; Ibers, J. A.; Poeppelmeier, K. R., *J. Solid State Chem.* **2012,** *192*, 34-37.

46. Gomez, V.; Fuhr, O.; Ruben, M., *CrystEngComm* **2016,** *18*, 8207-8219.

47. Tong, Y.-B.; Ren, L.-T.; Duan, H.-B.; Liu, J.-L.; Ren, X.-M., *Dalton Trans.* **2015,** *44*, 17850-17858.

48. Hodorowicz, M. A.; Piaskowska, A.; Stadnicka, K. M., *Acta Cryst. C* **2012,** *68*, m173-m176.

49. Billing, D. G.; Lemmerer, A., *CrystEngComm* **2006,** *8*, 686-695.

50. Niu, J.-P.; Zhai, Q.-G.; Luo, J.-H.; Li, S.-N.; Jiang, Y.-C.; Hu, M.-C., *Inorg. Chem. Commun.* **2011,** *14*, 663-666.

51. Zimmermann, I.; Keene, T. D.; Hauser, J.; Decurtins, S.; Liu, S.-X., *Acta Cryst. E* **2014,** *70*, 178-182.

52. Corradi, A. B.; Bruni, S.; Cariati, F.; Ferrari, A. M.; Saccani, A.; Sandrolini, F.; Sgarabotto, P., *Inorganica Chimica Acta.* **1997,** *254*, 137-143.

53. Chen, T.; Zhou, Y.; Sun, Z.; Zhang, S.; Zhao, S.; Tang, Y.; Ji, C.; Luo, J., *Inorg. Chem.* **2015,** *54*, 7136-7138.

54. Billing, D. G.; Lemmerer, A., *Acta Cryst. E* **2003,** *59*, m381-m383.

55. Kanatzidis, M. G., *Phosphorus Sulfur Silicon Relat Elem.* **1994,** *93*, 159-172.

56. Salim, T.; Sun, S.; Abe, Y.; Krishna, A.; Grimsdale, A. C.; Lam, Y. M., *J. Mater. Chem. A* **2015,** *3*, 8943-8969.

57. Lemmerer, A.; Billing, D. G., *CrystEngComm.* **2012,** *14*, 1954-1966.

58. Bonamartini Corradi, A.; Ferrari, A. M.; Righi, L.; Sgarabotto, P., *Inorg. Chem.* **2001,** *40*, 218-223.

59. Li, Y.; Zheng, G.; Lin, C.; Lin, J., *Cryst. Growth Des.* **2008,** *8*, 1990-1996.

60. Yaffe, O.; Guo, Y.; Tan, L. Z.; Egger, D. A.; Hull, T.; Stoumpos, C. C.; Zheng, F.; Heinz, T. F.; Kronik, L.; Kanatzidis, M. G.; Owen, J. S.; Rappe, A. M.; Pimenta, M. A.; Brus, L. E., *Phys. Rev. Lett.* **2017,** *118*, 136001.

61. Quarti, C.; Grancini, G.; Mosconi, E.; Bruno, P.; Ball, J. M.; Lee, M. M.; Snaith, H. J.; Petrozza, A.; De Angelis, F., *J. Phys. Chem. Lett.* **2014,** *5*, 279-284.

62. Nakamoto, K., *Infrared and Raman Spectra of Inorganic and Coordination Compounds*. Wiley: 1977.

63. Alonso, J.; Martinez-Lope, M.; Casais, M.; Fernandez-Diaz, M., *Inorg. Chem.* **2000,** *39*, 917-923.

64. Lufaso, M. W.; Woodward, P. M., *Acta Cryst. B* **2004,** *60*, 10-20.

65. Robinson, K.; Gibbs, G.; Ribbe, P., *Science* **1971,** *172*, 567-570.

66. Kamminga, M. E.; de Wijs, G. A.; Havenith, R. W. A.; Blake, G. R.; Palstra, T. T. M., *Inorg. Chem.* **2017,** *56*, 8408-8414.

67. Smith, M. D.; Watson, B. L.; Dauskardt, R. H.; Karunadasa, H. I., *Chem. Mater.* **2017,** *29*, 7083-7087.

68.   Wu, Z.; Li, L.; Ji, C.; Lin, G.; Wang, S.; Shen, Y.; Sun, Z.; Zhao, S.; Luo, J., *Inorg. Chem.* **2017,** *56*, 8776-8781.
69.   Mao, L.; Wu, Y.; Stoumpos, C. C.; Traore, B.; Katan, C.; Even, J.; Wasielewski, M. R.; Kanatzidis, M. G., *J. Am. Chem. Soc.* **2017,** *139*, 11956-11963.
70.   Dolomanov, O. V.; Bourhis, L. J.; Gildea, R. J.; Howard, J. A.; Puschmann, H., *J. Appl. Crystallogr.* **2009,** *42*, 339-341.
71.   Kortüm, G.; Braun, W.; Herzog, G., *Angew. Chem. Int. Ed.* **1963,** *2*, 333-341.
72.   de Mello, J. C.; Wittmann, H. F.; Friend, R. H., *Adv. Mater.* **1997,** *9*, 230-232.
73.   José, M. S.; Emilio, A.; Julian, D. G.; Alberto, G.; Javier, J.; Pablo, O.; Daniel, S.-P., *J. Phys. Condens. Matter* **2002,** *14*, 2745.
74.   Artacho, E.; Anglada, E.; Diéguez, O.; Gale, J. D.; García, A.; Junquera, J.; Martin, R. M.; Ordejón, P.; Pruneda, J. M.; Sánchez-Portal, D., *J. Phys. Condens. Matter* **2008,** *20*, 064208.
75.   Perdew, J. P.; Burke, K.; Ernzerhof, M., *Phys. Rev. Lett.* **1996,** *77*, 3865-3868.
76.   Troullier, N.; Martins, J. L., *Phys. Rev. B* **1991,** *43*, 1993-2006.
77.   Artacho, E.; Sánchez-Portal, D.; Ordejón, P.; García, A.; Soler, J. M., *Phys. Status Solidi B* **1999,** *215*, 809-817.
78.   Fernández-Seivane, L.; Oliveira, M. A.; Sanvito, S.; Ferrer, J., *J. Phys. Condens. Matter* **2006,** *18*, 7999.

TOC Graphic